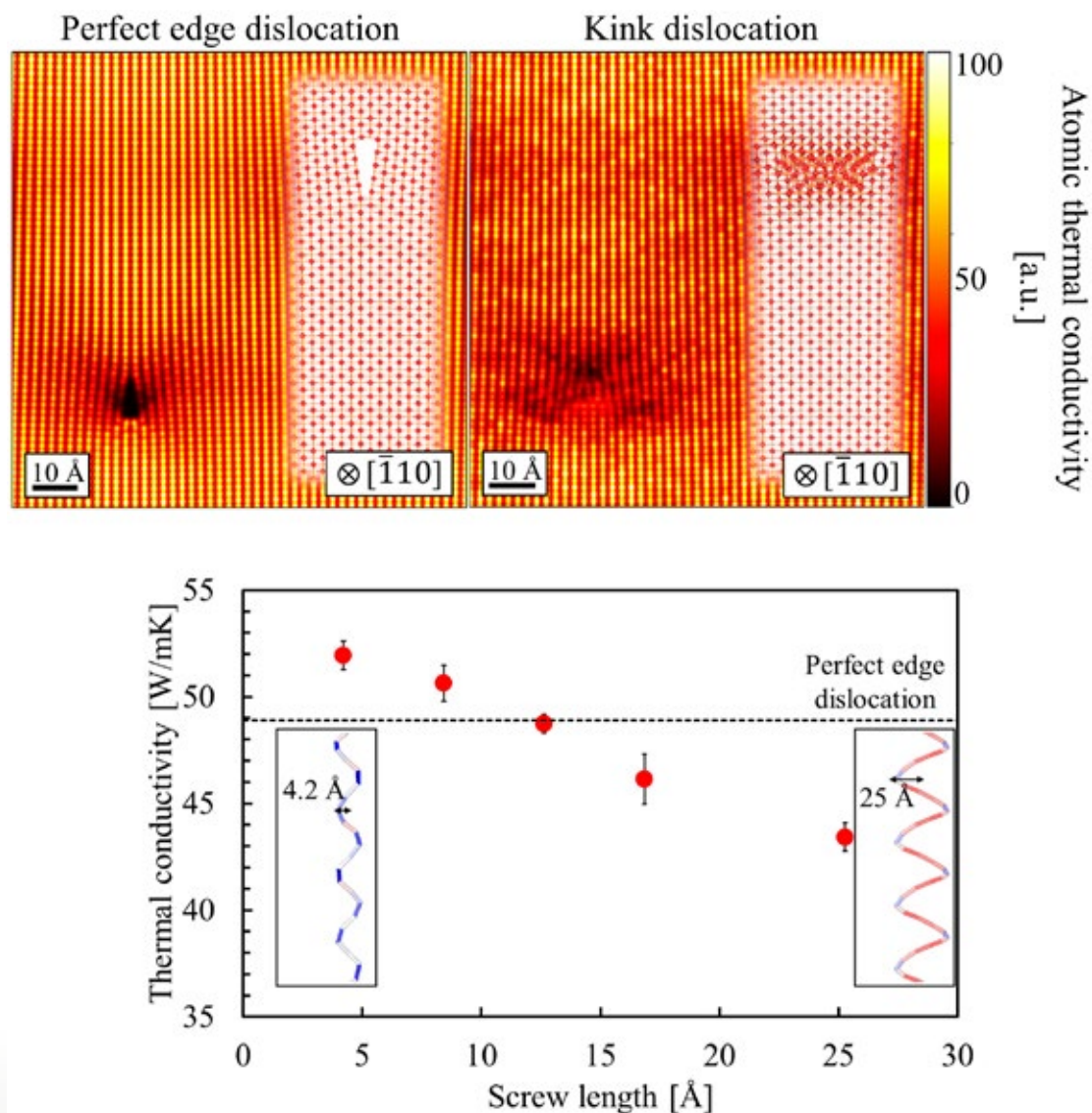


JCS-Japan

October
vol.131



Journal of the Ceramic Society of Japan

2023

FULL PAPER

Enhanced reduction of thermal conductivity across kink dislocation textures in magnesium oxide

Wataru Sekimoto^{1,†}, Susumu Fujii^{1,2} and Masato Yoshiya^{1,2}

¹Division of Materials and Manufacturing Science, Graduate School of Engineering, Osaka University, 2-1 Yamadaoka, Suita, Osaka 565-0871, Japan

²Nanostructures Research Laboratory, Japan Fine Ceramics Center, 2-4-1 Mutsuno, Atsuta, Nagoya 456-0871, Japan

Our understanding on how dislocation textures quantitatively affect thermal conductivity has been limited. We investigate the impact of kink dislocations on phonon thermal conduction in MgO by molecular dynamics, through changing edge and screw components in kink dislocations. The thermal conductivity is almost independent of the length of the edge component, but is rather reduced significantly with increasing the length of screw component, resulting in lower thermal conductivity than perfect edge dislocations. This reveals the combined effect of the edge and screw components on thermal conductivity beyond the simple description as one-dimensional obstacles and linear elastic strain field. Atomic contributions to thermal conductivity show that not only atoms in the vicinity of the kink dislocation cores but also those away from the cores exhibit suppressed thermal conductivity compared to the perfect edge dislocations. These results indicate that it is possible to efficiently reduce thermal conductivity in complex dislocation textures in real materials.

©2023 The Ceramic Society of Japan. All rights reserved.

Key-words : Thermal conductivity, Dislocations, Kink, Materials design, Molecular dynamics

[Received March 31, 2023; Accepted April 28, 2023]

1. Introduction

Dislocations, responsible for plastic deformation, are linear lattice defects and are ubiquitous in a wide spectrum of materials. Recently, many attempts have been made to control dislocations not only for mechanical properties but also for diverse material properties.¹⁾ For example, leakage currents caused by dislocations in InGaN-based LEDs,^{2),3)} improved dielectric and piezoelectric properties in perovskite oxides,^{4),5)} unusual magnetism⁶⁾ in BiFeO₃, and enhanced catalytic hydrogen evolution reactions⁷⁾ in MoS₂ have been reported.

Controlling thermal conductivity is critical for many applications, such as heat dissipation for high-power electronic devices⁸⁾ and heat insulation for thermoelectric materials.⁹⁾ Recently, dislocations were found to have a non-negligible impact on thermal conductivity. For example, the reduction of thermal conductivity has been reported for misfit dislocations at heterointerfaces, low-angle tilt grain boundaries as edge dislocation arrays, and twist grain boundaries as screw dislocation arrays.^{10)–13)} In addition to those geometrically-necessary dislocations (GN), statistically-stored dislocations (SS) also play an important role in thermal conduction.^{14),15)}

A series of pioneering study by Klemens proposed phonon scattering caused by dislocations based on a discrete lattice model with nonlinear elastic theory, in which dislocations are described by an column of vacancies and elastic strain fields.^{16),17)} Despite the importance of the pioneering studies, however, the capability to experimentally observe dislocation atomic structures and to control nanostructures has raised the shortcomings of oversimplified dislocation structures. For example, it has been shown that the thermal conductivity of arrayed GN dislocations, in other words, near low-angle tilt grain boundaries, is highly dependent on the atomic structure of the dislocations, and that dislocation cores with low atomic number density are effective in the reduction of thermal conductivity.¹⁸⁾ A model to predict thermal conductivity from the grain boundary atomic structures also show that small structural distortions near the GN dislocations can dramatically reduce thermal conductivity.¹⁹⁾

Compared with GN dislocations, our understanding on the suppression mechanism of thermal conductivity in SS dislocations has been limited. Only the impact of isolated perfect edge dislocations has been investigated,²⁰⁾ revealing that nonlinear strain fields in the vicinity of SS dislocation cores reduce thermal conductivity by interrupting the collective vibration of atoms. Here, to understand the impact of more realistic dislocations on thermal conduction, we performed a numerical analysis on kink dislocation textures. Kink dislocations are universally present in real materials; kink dislocations are formed during dis-

[†] Corresponding author: W. Sekimoto; E-mail: Wataru.Sekimoto@mat.eng.osaka-u.ac.jp

[‡] Preface for this article: DOI <https://doi.org/10.2109/jcersj2.131.P10-1>

location migration in materials due to the large Peierls barrier or due to dislocation cutting caused by interactions with forest dislocations. As kink dislocations include both edge and screw components (mixed dislocations), it is possible to reveal the impact of more realistic dislocation textures on thermal conductivity.

2. Methods

MgO was chosen as a model material in this study. Since the ionic radius of O atoms is larger than that of Mg atoms with the difference being similar to Fe and C in carbon steels, MgO can be considered to FCC O atoms with Mg atoms at its octahedral interstitial sites. Therefore, we can directly compare the results with other materials that have FCC sublattices and partially apply our findings to those materials.

A supercell with kink dislocations was constructed as follows: first, two crystal slabs with perfect edge dislocations were placed with dislocation line offset in the direction of the Burgers vector [Fig. 1(a)]. The dislocation length in the slabs (edge length) corresponds to the edge component and the offset of two slabs (screw length) corresponds to the screw component of kink dislocations [blue and red lines in Figs. 1(a) and 2(b)]. The kink dislocation core structures was obtained by optimizing atomic

arrangement in the supercell using the conjugate gradient and Newton-Raphson methods by General Utility Lattice Program code.²¹⁾ The pair-wise Buckingham potential²²⁾ was used in all cases. Then, two supercells with kink dislocations are placed adjacent to each other to form a new adjoined supercell in which two kink dislocations were positioned with the angle of 45° in the cell according to Peach-Koehler equation [Fig. 1(b)]. Eight kink models were constructed in total with different edge and screw lengths up to about 42 and 25 Å, respectively.

To determine the equilibrium cell lengths of each kink model at 300 K, molecular dynamics (MD) simulations were performed using the Large-scale Atomic/Molecular Massively Parallel Simulator (LAMMPS) code²³⁾ for 400 ps with velocity scaling²⁴⁾ under constant pressure condition (1.013×10^5 Pa). A timestep in MD simulations is set to 1 fs. With the fixed cell lengths, thermal equilibrium was then achieved at 300 K, by performing MD simulations for 100 ps with velocity scaling and for 300 ps with Nosé–Hoover thermostat^{25),26)} under constant volume conditions. (Note that, during MD simulations for a perfect screw dislocation model in MgO under finite temperature and 3D periodic boundary conditions, screw dislocation pair annihilation occurred as the strain fields between screw dislocations with opposite signs canceled out.)

To analyze thermal conductivity, perturbed MD²⁷⁾ was performed using custom-written code to LAMMPS package.²⁸⁾ In this method, the microscopic heat flux \mathbf{J} is determined at each atom by the sum of interactions from surrounding atoms and the atoms' own energy, given by

$$\begin{aligned} \mathbf{J} &= \sum_i \mathbf{J}_i \\ &= \sum_i \frac{1}{2V} \left[\left\{ m_i \mathbf{v}_i^2 + \sum_j \phi_{ij} \right\} \mathbf{I} \cdot \mathbf{v}_i - \sum_j (\mathbf{F}_{ij} \cdot \mathbf{v}_i) \mathbf{r}_{ij} \right] \end{aligned} \quad (1)$$

where m_i and \mathbf{v}_i are mass and velocity of atom i , ϕ_{ij} denotes internal energy determined by interatomic interaction, V is volume of a supercell, \mathbf{F}_{ij} is a force exerted from atom j to atom i , $\mathbf{r}_{ij} = \mathbf{r}_j - \mathbf{r}_i$ with \mathbf{r}_i being a position of atom i , and \mathbf{I} is a unit tensor of second rank. Thermal conductivity is obtained as a function of the time-averaged microscopic heat flux, and the thermal conductivity κ_{ph} of the entire system is given as the sum of atomic thermal conductivities calculated from the average heat flux of each atom²⁹⁾ by

$$\kappa_{\text{ph}} = \sum_i \kappa_i = \sum_i \frac{1}{\mathbf{F}_{\text{ext}} T} \lim_{t \rightarrow \infty} \langle J_i \rangle_t \quad (2)$$

where T is target temperature of a system and \mathbf{F}_{ext} is a small amount of perturbation determined by the microscopic heat flux. Thus, the contribution of each atom to the overall thermal conductivity can be decomposed without any ambiguity. This allows us to map the atomic thermal conductivities around the kink dislocations. Further details of thermal conductivity calculations are explained elsewhere.^{18),20),27),29),30)}

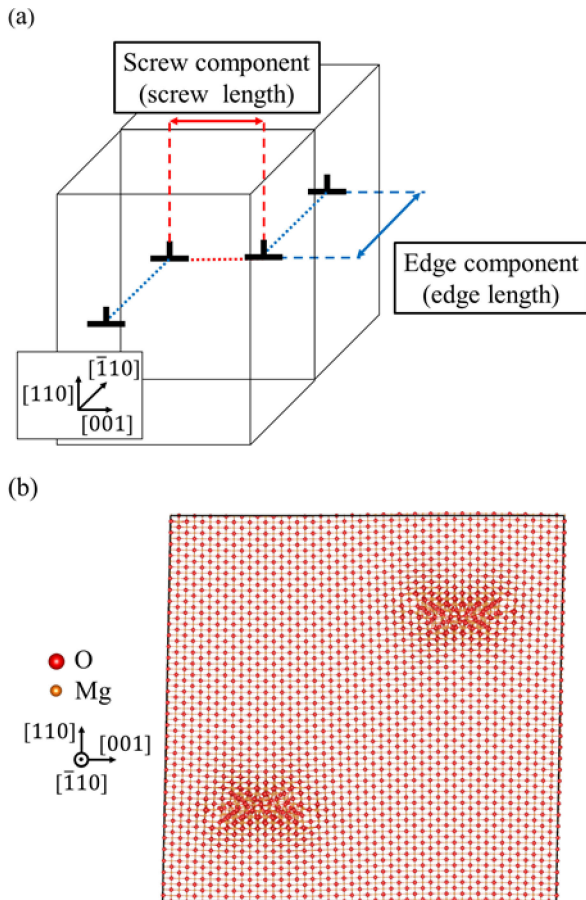


Fig. 1. Schematic illustration of the simulation box. (a) Arrangement of edge dislocation cores and lengths of edge and screw components before optimization. (b) An example of kink dislocation model used for thermal conductivity calculations.

In this study, thermal conductivities were measured for 4 ns with three different magnitude of perturbations within the linear response regime. The direction of calculated thermal conductivity is across the kink dislocation line [001] because thermal conductivity of this direction is greater contributions for the suppression of thermal conductivity, thus a guide to exploit kink dislocations (See Fig. S1 in the Supplementary Materials).

3. Results and discussion

Figure 2 shows an example of kink dislocation structure. The edge and screw components cannot be clearly identified as in real kink textures because their intersection angles are not 90° as shown in Fig. 1(a). The structure with high edge components on the blue line is similar to the perfect edge dislocation core structures. On the other hand, the structures with screw components on the red line (mixed dislocation) has a distorted atomic arrangement compared with the perfect edge dislocation, to minimize the total energy of kink dislocation. For simplicity, the lengths of the edge and screw components are estimated from the structures before optimization [specified in Fig. 1(a)].

Table 1 compares thermal conductivity of perfect crystal, column of vacancies, edge dislocations and kink dislocations at almost the same dislocation density. As can be seen from the Table 1, overall thermal conductivity is significantly suppressed by the dislocations despite the fact that they are linear defects instead of planar defects which are more likely to disturb the wave propagations. The thermal conductivity of kink dislocations varies depending on the edge and screw components.

Figure 3 shows the dependences of the thermal conductivity on edge component [Fig. 3(a)] and screw component [Fig. 3(b)] in kink dislocations. With a fixed screw length at 8 \AA [Fig. 3(a)], the thermal conductivity of kink dis-

location models is almost equal to that of the perfect edge dislocation, regardless of the edge length. This indicates that the impact of screw component on thermal conduction is not significant when its length is relatively short. On the other hand, with a fixed edge length of 6 \AA [Fig. 3(b)], the thermal conductivity significantly decreases as the screw length increases. In particular, when the screw length is as long as 25 \AA , the thermal conductivity suppressed by about 10% less than the perfect edge dislocation.

To understand the impact of these kink dislocations on thermal conductivity, we analyzed the variation (standard deviation) of bond length as a parameter of structural distortion for the perfect edge dislocation and eight kink models (**Fig. 4**). The results show that there is a negative correlation between the variation of bond length and ther-

Table 1. Overall thermal conductivity of perfect crystal and three models with different dislocation structures. Their dislocation density is about $2 \times 10^{16} \text{ m}^{-2}$. Thermal conductivity dependence on dislocation density for edge dislocations are found in Ref. 20)

model	Thermal conductivity [W/mK]
Perfect crystal ²⁰⁾	142
column of vacancies	70.1
Edge dislocation ²⁰⁾	48.9
Kink dislocations	43.4–51.9

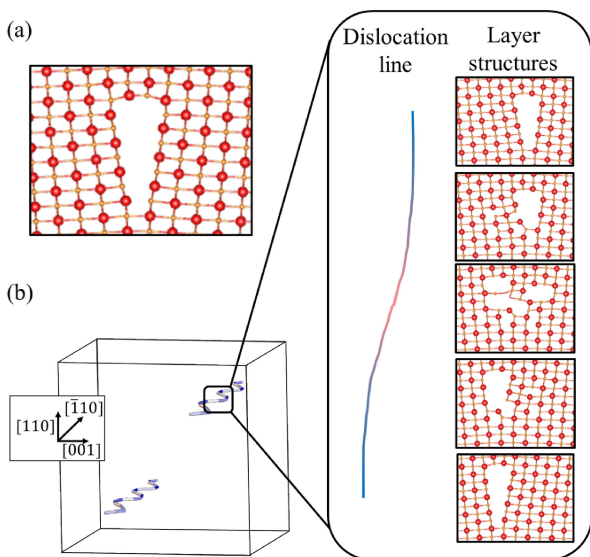


Fig. 2. The core structures of (a) perfect edge dislocation and (b) each layer along a kink dislocation, associated with its line shape.

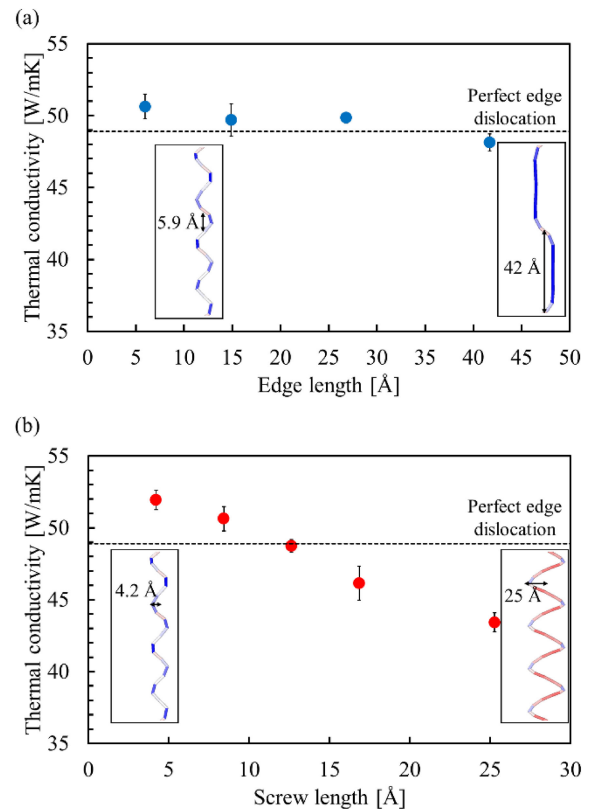


Fig. 3. Thermal conductivity as a function of (a) edge length and (b) screw length. The screw and edge length are fixed to about 8 \AA and 6 \AA in (a) and (b), respectively. The thermal conductivity with perfect edge dislocation is also shown as a dashed line.

mal conductivity. Kinks with long screw length have a large variation in bond length and low thermal conductivity, while those with short screw lengths have a small variation in bond length and relatively high thermal conductivity (equal to that of the perfect edge dislocation). This indicates that the structural distortion in the mixed dislocations with edge and screw components further suppress thermal conductivity compared with the perfect edge dislocation.

To investigate the suppression mechanism of thermal conduction in the vicinity of kink dislocation cores, the atomic thermal conductivities were calculated and projected onto ($\bar{1}10$) two dimensional planes for the models with the perfect edge dislocations and kink dislocations, with the same relative position of the dislocation line (Fig. 5). For both dislocations, the atomic thermal conductivity decreased significantly not only in the vicinity of the dis-

location core but also in the regime away from them. The disordered kink structure resulted in non-uniform atomic thermal conductivities than the perfect edge dislocation, leading to more significant suppression of overall thermal conduction.

For more quantitative understanding, the averaged atomic thermal conductivities in the vicinity of the dislocation cores and in the regime away from them were calculated (Fig. 6). The kink dislocations reduced the thermal conductivity both in the vicinity of the dislocation cores and the regime away from them than perfect edge dislocations. Compared to the perfect edge dislocation, the decrease was about 6 W/mK in the vicinity of the dislocation cores and 5 W/mK in the region away from them. This indicates that the kink dislocations not only affect the thermal conduction of atoms whose coordination environment is modified by the dislocation core structures, but also the thermal conductivity of atoms around the dislocation core. The changes in the local coordination environment due to the kink rearrangement suppresses phonon conduction, which is a collective vibration, in a broad spatial range.

4. Conclusions

We analyzed the impact of edge and screw dislocations on thermal conduction in MgO kink dislocation textures using perturbed MD. The significant suppression of thermal conduction in kink dislocations originates from the combined impact of the edge and screw dislocations, resulting in lower thermal conductivity than perfect edge dislocations. It was found that thermal conduction is scattered not only for atoms in the vicinity of the kink dislocation core but also for those away from the dislocation line. Thus, complex dislocation textures as seen in real materials may reduce thermal conductivity more drastically.

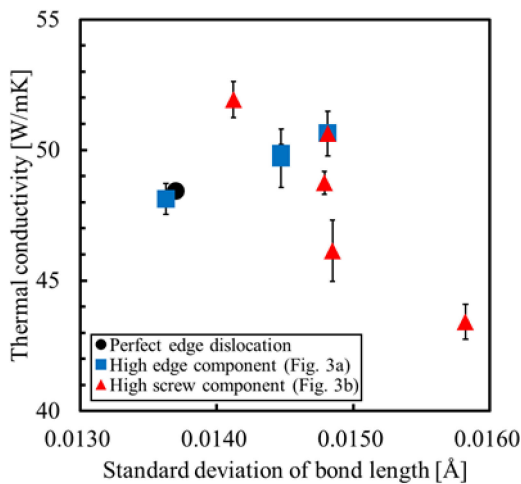


Fig. 4. Variation of bond length and thermal conductivity in a perfect edge dislocation and eight kink dislocation models.

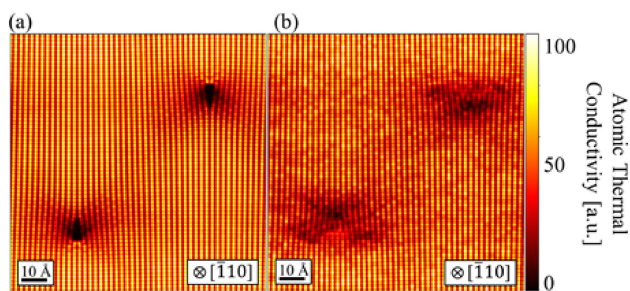


Fig. 5. Two dimensional maps of atomic thermal conductivities in (a) perfect edge dislocation model and (b) kink dislocation model (edge and screw length are about 6 and 25 Å).

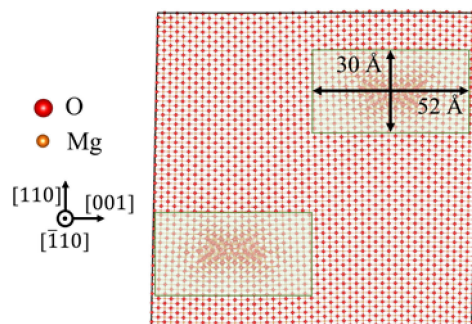


Fig. 6. The regime defined as the vicinity of dislocation cores used for averaging atomic thermal conductivities in Table 2.

Table 2. Atomic thermal conductivities averaged in the vicinity of dislocation core and regime away from dislocation core for perfect and kink (edge length: 6 Å, screw length: 25 Å) dislocation

	The vicinity of dislocation cores		Away from dislocation cores	
	number of atoms	Thermal conductivity [W/mK]	number of atoms	Thermal conductivity [W/mK]
Perfect edge	6888	40.4	26250	52.8
Kink	7846	34.7	30078	47.7

Acknowledgements This study is supported by Grant-in-Aid for JSPS Fellows [Grant Number: JP22J20564] and Grant-in-Aid for Scientific Research on Innovative Areas ‘New Materials Science on Nanoscale Structures and Functions of Crystal Defect Cores’ [Grant Number: JP19H05786]. SF was also supported by Grant-in-Aid for Scientific Research [Grant Numbers: JP20H05195 and JP20K15034]. MY was also supported by Grant-in-Aid for Scientific Research [Grant Number: JP20K05062].

References

- 1) K. Matsunaga, M. Yoshiya, N. Shibata, H. Ohta and T. Mizoguchi, *J. Ceram. Soc. Jpn.*, **130**, 648–667 (2022).
- 2) L. Van Deurzen, M. Gómez Ruiz, K. Lee, H. Turski, S. Bharadwaj, R. Page, V. Protasenko, H. Xing, J. Lähnemann and D. Jena, *J. Phys. D Appl. Phys.*, **54**, 495106 (2021).
- 3) I. Belabbas, G. P. Dimitrakopoulos, J. Kioseoglou, J. Chen and J. Smalc-Koziorowska, *Model. Simul. Mater. Sc.*, **30**, 085004 (2022).
- 4) M. Höfling, X. Zhou, L. M. Riemer, E. Bruder, B. Liu, L. Zhou, P. B. Groszewicz, F. Zhuo, B.-X. Xu, K. Durst, X. Tan, D. Damjanovic, J. Koruza and J. Rödel, *Science*, **372**, 961–964 (2021).
- 5) N. Li, R. Zhu, X. Cheng, H. J. Liu, Z. Zhang, Y. L. Huang, Y. H. Chu, L. Q. Chen, Y. Ikuhara and P. Gao, *Scripta Mater.*, **194**, 113624 (2021).
- 6) E. A. Volnistem, L. Macková, R. F. Muniz, F. R. Estrada, S. M. de Nóbrega, G. S. Dias, V. F. Freitas, L. F. Cótica and I. A. dos Santos, *J. Alloy. Compd.*, **887**, 161421 (2021).
- 7) S. Wang, L. Wang, L. Xie, W. Zhao, X. Liu, Z. Zhuang, Y. Zhuang, J. Chen, S. Liu and Q. Zhao, *Nano Res.*, **15**, 4996–5003 (2022).
- 8) S. Deng, X. Zhang, G. D. Xiao, K. Zhang, X. He, S. Xin, X. Liu, A. Zhong and Y. Chai, *Nanotechnology*, **32**, 315710 (2021).
- 9) Y. Zhu, Z. Han, B. Han, F. Jiang, X. Wu, C. G. Han, Y. Deng and W. Liu, *ACS Appl. Mater. Inter.*, **13**, 56164–56170 (2021).
- 10) Y. Li, Z. Zheng, A. Diaz, S. R. Phillpot, D. L. McDowell and Y. Chen, *Acta Mater.*, **237**, 118143 (2022).
- 11) J. Wang, Y. Yu, J. He, J. Wang, B. Ma, X. Chao, Z. Yang and D. Wu, *ACS Appl. Energ. Mater.*, **4**, 14608–14617 (2021).
- 12) R. Gurunathan, R. Hanus, S. Graham, A. Garg and G. J. Snyder, *Phys. Rev. B*, **103**, 144302 (2021).
- 13) Y. Ran, Z. Lu, X. Zhang, W. Li, B. Duan, P. Zhai and G. Li, *Appl. Phys. Lett.*, **119**, 161601 (2021).
- 14) M. Johanning, L. Porz, J. Dong, A. Nakamura, J. F. Li and J. Rödel, *Appl. Phys. Lett.*, **117**, 021902 (2020).
- 15) Y. Sun, Y. Zhou, J. Han, W. Liu, C. Nan, Y. Lin, M. Hu and B. Xu, *NPJ Comput. Mater.*, **5**, 1–6 (2019).
- 16) P. G. Klemens, in “Solid State Phys.”, Ed. by F. Seitz and D. Turnbull, Academic Press (1958) pp. 1–98.
- 17) P. G. Klemens, *Proc. Phys. Soc. A*, **68**, 1113–1128 (1955).
- 18) S. Fujii, T. Yokoi and M. Yoshiya, *Acta Mater.*, **171**, 154–162 (2019).
- 19) S. Fujii, T. Yokoi, C. A. J. Fisher, H. Moriwake and M. Yoshiya, *Nat. Commun.*, **11**, 1854 (2020).
- 20) W. Sekimoto, S. Fujii and M. Yoshiya, *Scripta Mater.*, **202**, 113991 (2021).
- 21) J. D. Gale, *J. Chem. Soc. Faraday T.*, **93**, 629–637 (1997).
- 22) F. Landuzzi, L. Pasquini, S. Giusepponi, M. Celino, A. Montone, P. L. Palla and F. Cleri, *J. Mater. Sci.*, **50**, 2502–2509 (2015).
- 23) S. Plimpton, *J. Comput. Phys.*, **117**, 1–19 (1995).
- 24) L. V. Woodcock, *Chem. Phys. Lett.*, **10**, 257–261 (1971).
- 25) S. Nosé, *Mol. Phys.*, **52**, 255–268 (1984).
- 26) W. G. Hoover, *Phys. Rev. A*, **31**, 1695–1697 (1985).
- 27) M. Yoshiya, A. Harada, M. Takeuchi, K. Matsunaga and H. Matsubara, *Mol. Simulat.*, **30**, 953–961 (2004).
- 28) S. Fujii, M. Yoshiya and C. A. J. Fisher, *Sci. Rep.-UK*, **8**, 2–4 (2018).
- 29) M. Tada, M. Yoshiya and H. Yasuda, *Proc. Phys. Soc. A*, **68**, 1113–1128 (1955).
- 30) S. Fujii and M. Yoshiya, *J. Electron. Mater.*, **45**, 1217–1226 (2016).